applied sciences

MDPI

Article

Chiral-Lattice-Filled Composite Tubes under Uniaxial and Lateral Quasi-Static Load: Experimental Studies

Kadir Gunaydin [1,*], Aykut Tamer [2], Halit Suleyman Turkmen [3], Giuseppe Sala [1] and Antonio Mattia Grande [1]

[1] Department of Aerospace Science and Technology, Politecnico di Milano, via La Masa 34, 20156 Milano, Italy; giuseppe.sala@polimi.it (G.S.); antoniomattia.grande@polimi.it (A.M.G.)
[2] Department of Mechanical Engineering, Imperial College London, London SW7 2AZ, UK; a.tamer@imperial.ac.uk
[3] Faculty of Aeronautics and Astronautics, Istanbul Technical University, Istanbul 34467, Turkey; halit@itu.edu.tr
* Correspondence: kadir.gunaydin@polimi.it

Abstract: Our research investigated the energy absorption characteristics of chiral auxetic lattices filled cylindrical composite tubes subjected to a uniaxial and lateral quasi-static load. The lattice structures were manufactured using a 3D printing technique. Carbon fiber composite tubes without filler material were initially subjected to uniaxial and lateral quasi-static crushing load. The same types of experiment were then performed on chiral lattices and chiral lattices filled composite tubes. For the different cases, the load–displacements curves were analyzed and the specific energy absorption (SEA) values were compared. The SEA capability for the axial quasi-static crushing of the chiral lattices filled composite tubes decreased in comparison with the hollow composite design. However, the most significant result was that the average SEA value in the case of lateral loading increased dramatically in comparison with the hollow composite configuration.

Keywords: composite tube; chiral auxetics; 3D printing; energy absorption; crushing

check for updates

Citation: Gunaydin, K.; Tamer, A.; Turkmen, H.S.; Sala, G.; Grande, A.M. Chiral-Lattice-Filled Composite Tubes under Uniaxial and Lateral Quasi-Static Load: Experimental Studies. *Appl. Sci.* **2021**, *11*, 3735. https://doi.org/10.3390/app11093735

Academic Editors: Marwan Al-Haik and David Barton

Received: 27 February 2021
Accepted: 16 April 2021
Published: 21 April 2021

Publisher's Note: MDPI stays neutral with regard to jurisdictional claims in published maps and institutional affiliations.

Copyright: © 2021 by the authors. Licensee MDPI, Basel, Switzerland. This article is an open access article distributed under the terms and conditions of the Creative Commons Attribution (CC BY) license (https://creativecommons.org/licenses/by/4.0/).

1. Introduction

Energy-absorbing structures are encountered in many real-life situations, which involves an exchange of compressive loads between two or more objects. Critical equipment or occupants should be protected from the resulting energy transfer using dedicated components that absorb the crush energy. Composite materials have been extensively used in recent years for energy absorption applications because of their lightweight, corrosion resistance and high energy absorption characteristics [1]. When designed accordingly, composite materials crush under the compressive load and therefore absorb a significant amount of energy transfer that stems from compressive loads. For example, in the automotive and aerospace industry, thin-walled tubes with different types of filler are commonly used as passive energy-absorbing sacrificial structures [2,3]. Composite tubes for energy absorption applications are positioned to bear the load in the uniaxial direction, however, in some applications such as helicopter skid landing gears, lateral loading is necessary in addition to bending loads [4].

The design of passive energy-absorbing structures, such as tubes, aims to dissipate a fixed amount of energy by crushing at an invariable load over an increasing stroke (crushing distance) without exhausting the crushing stroke. In the case of consuming all stroke, i.e., when the tube "bottoms out", high peak loads emerge [5]. The high peak loads and violent fluctuations in loads increase the risk of whiplash [6]. To prevent this undesirable consequence and increase energy absorption capacity, auxetic materials have been considered [7]. Thanks to their negative Poisson's ratio, auxetic materials are useful in energy absorption since they accumulate more material under the crush region as opposed to conventional materials.

Numerous studies have been conducted to understand and identify the crushing behavior of composite materials, and especially their failure mechanisms, which heavily depend upon the fiber and matrix properties [8–10]. A significant number of studies have also appeared in the literature about the effect of the stacking sequence [11–14]. Jacob et al. [1] suggested that the overall energy absorption increases when fibers parallel to the loading direction were laterally supported, such as in the case of the [0/90/0/90] s layup. Besides unidirectional composites, the energy absorption and damage resistance capabilities of 3D woven composites under crushing load after multiple impacts [15] and the effect of different architectures of 3D carbon fiber woven composites were investigated [16].

Several design aspects are also critical in the crush resistance of composites. Tubes with chamfered, inward folding or outward-splaying crush-caps, or the combination of the two (chamfered-end and crush-cap) were investigated as designs with potential embedded failure triggering mechanisms. The objective of the trigger mechanism is to create a local region to elevate stress at one tip of the tube for failure initiation and disseminate it to the rest of the tube. As a result, the stable progressive crushing is promoted while an instant catastrophic failure is avoided.

Geometric aspects, such as the tube thickness (t) and the outer diameter (D), have been mentioned as important parameters related to the energy absorption and deformation modes of carbon fiber/PEEK composite tubes [17–19]. Farley [20] showed the presence of a nonlinear variation of the energy absorption versus D/t ratio. Hamada and Ramakrishna [21] observed that higher specific energy absorption (SEA) could be obtained using 2–3 mm thickness tubes. Gupta et al. [22] also demonstrated that one can prevent the global buckling and the catastrophic failure of axially crushed composite circular cross-section tubes by maintaining the D/t ratio between 15 and 40. The crush tube length is another critical parameter, which should be determined by considering the crash speed. If the crash velocity is too high, the crushing stroke can be insufficient and a high peak load can arise. In this case, either the crush tube length needs to be extended or a filler material must be used, such as foam and lattice structures.

Auxetic materials are classified as mechanical metamaterials because of their artificial and highly tailorable properties, which also include negative stiffness (exhibiting increasing displacement under decreasing load) or a negative coefficient of thermal expansion. The auxetic properties may be obtained using a wide selection of geometries, each may be customized to provide a specific performance (such as improved vibration damping or acoustic insulation). More information about the classification of auxetic structures (such as woven, foam or lattice structures) can be found in literature [23–25]. Recently, metamaterials with auxetic properties have gained attention because of their superior energy-absorbing characteristics and vibration-damping capabilities [26–30]. Scarpa et al. [29,31] observed in quasi-static and vibration tests that anti-tetra chiral lattices could constitute excellent design platforms for energy dampers.

Recently, auxetic lattice geometries were found to provide significant crush resistance and energy damping under compression in its in-plane direction, in which auxeticity is experienced. Gunaydin et al. [32,33] studied experimental and numerical crushing analysis of re-entrant and anti-tetrachiral auxetic lattices. Zhang et al. [34] numerically evaluated the dynamic crushing behavior of auxetic honeycombs with various cell-wall angles under different levels of crush loading. Ingrole et al. [7] compared the in-plane compressive properties of honeycomb, re-entrant auxetic, auxetic-strut and two different auxetic-strut/honeycomb hybrid cell structures. As these studies are confined to only-auxetic behavior, few experimental studies investigated the relationship of auxetic structures with composite tubes [35,36]. Recently, Simpson and Kazanci [37] investigated the crush response of auxetic lattices filled metal tube under the uniaxial compressive load.

This research proposes an innovative concept for the energy absorption improvement of composite crashboxes in the case of lateral loading. The concept is based on the contraction of the cellular structures in the composite tube with negative Poisson's ratio under lateral compressing loads to potentially increase the crush performance of composite tubes.

To demonstrate the concept experimentally, the chiral lattices were manufactured using a 3D printing facility; the carbon fiber composite tubes were supplied from a manufacturer. Chiral lattices, composite tubes (hollow) and chiral lattices filled composite tubes were axially and laterally compressed between two rigid plates during the quasi-static test process. There crush experiments were conducted for each group at least three times to show repeatability. The specific energy absorption, peak load, average (mean) crushing load, crushing efficiency and stroke efficiency were then calculated for each group. Finally, the results then compared to understand whether auxetic structures could be beneficial as a filler in designing efficient composite crushing tubes.

2. Method

This section explains the crushing theory, manufacturing of the specimens and test setup.

2.1. Crushing Theory

A brief discussion is necessary to explain the characteristics and experimental parameters about the energy absorption of structures for crashworthiness applications. The load-deflection diagrams characterize the energy absorption capacity of crashworthy structures and can be divided into three phases: pre-crushing, progressive crushing and densification. These stages can be seen in Figure 1, which shows the typical load (P) vs displacement (δ) behavior of energy-absorbing structures. The amount of energy absorption is the least in the pre-crushing stage, which is mostly characterized by elastic deformation [38]. Following PRE is the progressive crushing zone, as the material deforms further. The vast portion of energy is absorbed during this phase, in which permanent deformation and fracture occur. Thus, a longer progressive crushing zone suggests a higher energy absorption. The last phase is the densification phase in which the structure is fully compressed until it behaves like a rigid body and produces a higher resistance that can rise to over the testing system capacity [39]. For this reason, absorbed energy during the densification is excluded from the energy absorption calculations and all crushing behavior indicators used in this work cover the region of pre-crushing and progressive crushing zones as suggested in [3].

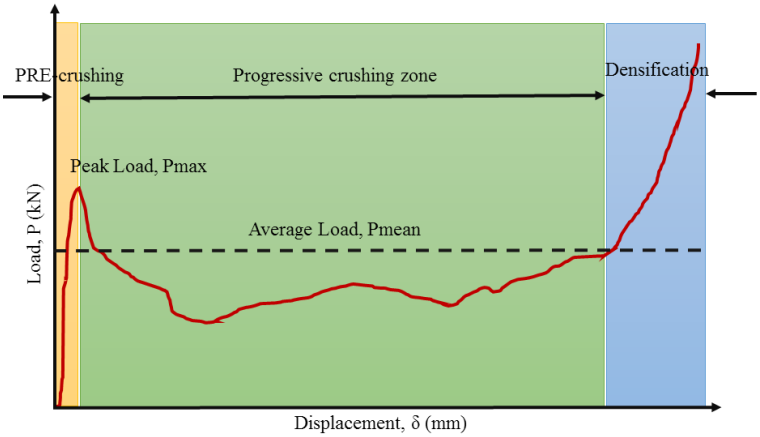


Figure 1. Energy absorption stages explained on load–displacement curve.

An important indicator of material energy absorption is the specific energy absorption (SEA) [39]. SEA is defined as the absorbed energy (AE) per unit mass of the crushed specimen, and indicated by the area under the load–displacement curve:

$$\text{SEA (J/kg)} = \frac{\text{energy absorbed (AE)}}{\text{mass of absorbent structure (m)}} = \frac{\int_0^{max} P(\delta)d\delta}{m} \quad (1)$$

where P, δ and m represent the load, displacement and specimen mass, respectively.

Another indicator of material crushing performance is the crushing force efficiency (CFE) [39], which is also known as the load uniformity ratio. The lower values of CFE

address the severe load fluctuations in the progressive crushing zone and/or relatively high peak load, which is an undesirable behavior. CFE is the ratio of the average crushing load (*MCF*, the mean load during the collapse) to peak load (*PCF*, highest load experienced during a crushing event):

$$CFE = \frac{MCF}{PCF} \tag{2}$$

Based on the discussions above, the onset of densification should be identified. For this purpose, we propose an energy efficiency parameter, $\eta(\delta)$:

$$\eta(\delta) = \frac{1}{P(\delta)} \int_0^{\delta} P(\delta) d\delta \tag{3}$$

By using the energy efficiency in Equation (3), a representative onset deflection of densification, d, can be numerically and consistently defined by obtaining the energy efficiency–deflection plot and selecting the highest point [40], as expressed in Equation (4):

$$\left. \frac{d\eta(\delta)}{d\delta} \right|_{\delta=d} = 0. \tag{4}$$

2.2. Manufacturing and Materials

2.2.1. Chiral Structure

Additive manufacturing (AM) is a modern production method to fabricate metamaterials. Layered manufacturing (LM) is the most common technique in AM for design verification, visualization and kinematic functionality testing [41,42]. Several LM techniques are available, such as laser powder bed fusion (LPBF), fused deposition modeling (FDM), stereolithography (SLA) and three-dimensional printing (3DP) [43]. Fused deposition modeling is commonly used because FDM printers and consumable materials are cheaper compared to the other mentioned 3D printing methods. In particular, *Zortrax™M200* 3D printer and *Zortrax™ABS* (Acrylonitrile Butadiene Styrene) plastics were employed in this study.

'NX 12: Siemens PLM™' Software was used to create the solid model of the lattices, which were then converted into an STL file imported into the 3D printer through the Z-Suite software. All specimens were printed at 90° raster orientation that is parallel to the building plate. The thickness of the layer was selected as 0.09 mm, with maximum infill to avoid spaces, normal seam and no material support used. The chiral structure was produced along the out-of-plane perpendicular direction of the lattice as seen in Figure 2. In this way, it was possible to prevent the use of support material, which is problematic to trim and remove without damaging the primary model.

The manufactured chiral structure consisted of 10 cells (Figure 2) due to the chiral lattice topology design according to the study of Alderson et al. [44], and FDM printer limits for maintaining the auxeticity as long as possible under the deformation. The elastic deformation of chiral structures starts with the rotation of nodes, and then ligaments start to wrap around the nodes. This rotating deformation mechanism forms the auxetic behavior [45]. The out-of-plane geometry of the chiral lattices is illustrated in Figure 3, and in-plane directions were shown on a coordinate system. The parameter R describes the minimal distance between the centers of two nodes, which is also an important parameter for manipulating the stiffness of the cell with the node outer radius, r_o and ligament thickness, t. The viable minimum wall thickness using *Zortrax™M200* 3D printer is 0.45 mm with a standard nozzle diameter of 0.4 mm. To provide better dimensional tolerance and fortify the ligaments the wall thickness was selected as twice of the minimum thickness that the 3D printer is capable of. The extrusion height of the chiral structure is denoted by H, and for the SEA value, the mass of the structure is an important parameter. See Table 1 for a detailed description of the chiral cell parameters and measured physical properties. Additionally, tensile specimens were produced according to EN ISO 527-3:2018

standard [46] to determine the ABS stress–strain data and observe the behavior of the ABS. All tensile specimens were printed at 90° raster orientation.

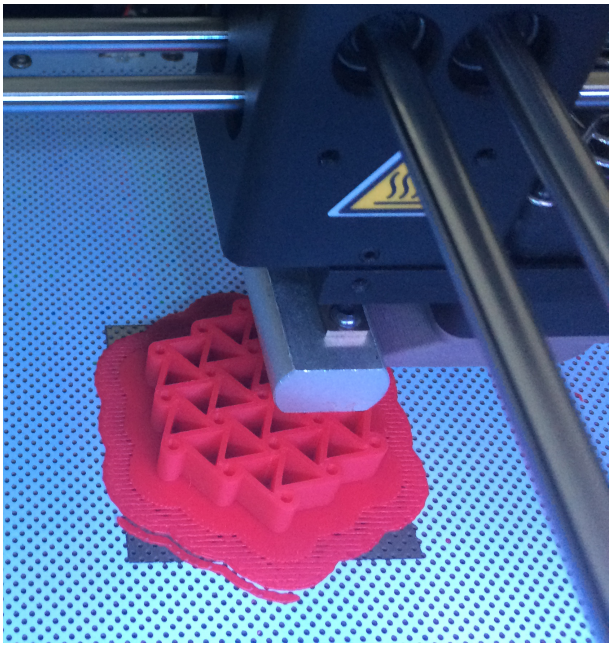


Figure 2. The production stage of the hexachiral lattice.

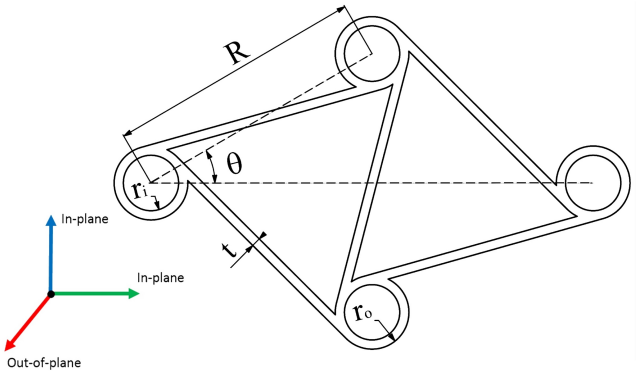


Figure 3. Parameters defining the topology of a chiral structure.

Table 1. Design parameters and physical properties of the chiral lattice structure.

R (mm)	r_o (mm)	r_i (mm)	θ (°)	H (mm)	Mass (g)
10.50	2.20	1.30	30	100	54.61

2.2.2. Composite Tubes

Commercial tubes were supplied by a manufacturer, which are filament wound composite tubes with a thermoset resin and stacking sequence of [0/±45/−90]. The mechanical properties are reported in Table 2. For the layup of the composite tube, the review study of Jacob et al. [1] was considered based on the energy absorption characteristics of composite tube design. The thickness, length and radius of the tube are determined based on [19–22]. The representation of the hollow tubes is presented in Figure 4, and design parameters are reported in Table 3. The ends of the tubes were cut out to ensure that the tubes are free from burrs or uneven edges. No other additional processes were applied to the ends of tubes. Moreover, no trigger mechanism was used in the tests, with both ends of the tubes being flat.

Table 2. Mechanical properties of the CFRP tube's base material.

Property	Units	Value
Tensile strength (axial)	MPa	734.9
Tensile strength (transverse)	MPa	16.3
Tensile modulus (axial)	GPa	73.0
Tensile modulus (transverse)	GPa	6.6
Compressive strength (axial)	MPa	227.8
Compressive strength (transverse)	MPa	39.4
Compressive modulus (axial)	GPa	36.9
Compressive modulus (transverse)	GPa	2.5
Poisson ratio (axial)	-	0.26
Poisson ratio (transverse)	-	0.03

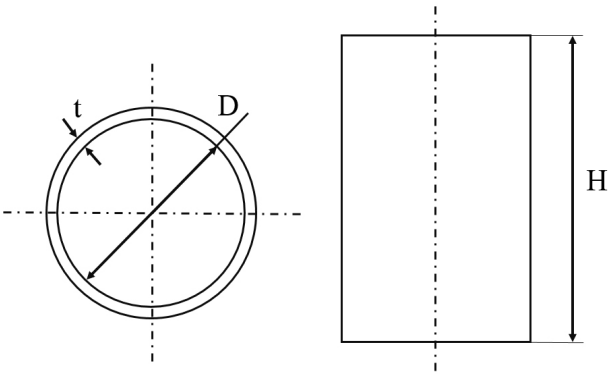


Figure 4. Parameters defining the topology of the hollow composite tube.

Table 3. Hollow composite tube design parameters.

D (mm)	H (mm)	t (mm)	Mass (g)
50	100	2	39.46

2.2.3. Chiral-Filled Composite Tubes

The FDM printed chiral structure was placed into the composite tube of the same length as presented in Figure 5 without using adhesives or binder. The outbox diameter of the chiral structure was kept slightly less than the inner diameter of the composite tube, enabling the relative motion of the chiral. The total mass of the assembly is 94.07 g, which is the sum of the mass of the chiral structure (54.61 g) and the hollow tube (39.46 g).

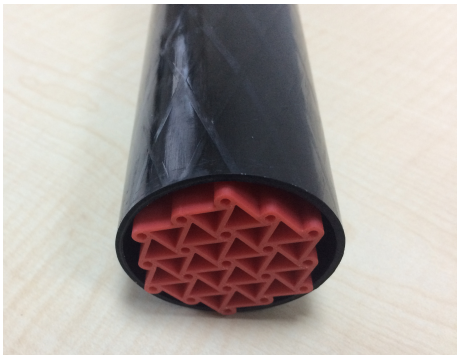


Figure 5. Chiral structure filled composite tube.

2.3. Test Setup

Tensile tests were carried out using an INSTRON™5980 100 kN universal Testing System with AVE 2 non-contacting video extensometer and its own commercial DIC

software. The quasi-static in-plane and out-of-plane crushing tests were also conducted using the same universal testing system as utilized in tensile tests with a crushing rate of 10 mm min^{-1}. This rate value was selected according to [47]. Load variation and the displacement of the crosshead values were recorded. Both lateral and uniaxial loading for the filled tube is seen in Figure 6. In all uniaxial out-of-plane crush tests, the approximate progression of crosshead was set to 80 mm. For the lateral tests, 25 mm progression was decided initially; however, due to the quick reach of the densification phase and instant load increase in this phase, the progression was reduced to 20 mm for in-plane compression of the chiral structures considering the emergence of instant high peak load, which can damage the load cell.

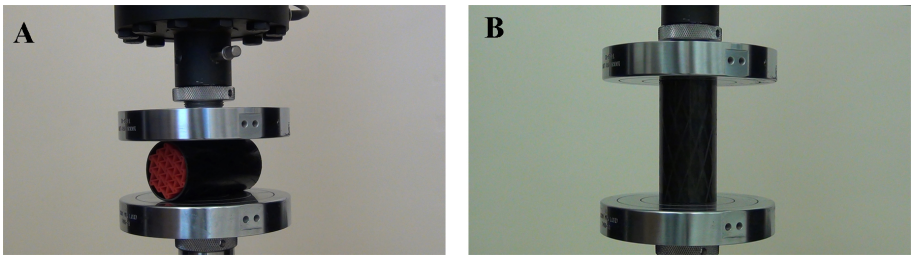


Figure 6. Lateral (**A**) and uniaxial (**B**) crushing of the auxetic structure filled composite tube.

3. Experiments and Results

3.1. Property Identification

The base ABS plastic properties were initially determined from six tensile tests performed at a rate of 5 mm/min. The stress–strain curves from the tensile test were obtained with good repeatability as shown in Figure 7. In addition, most of the ABS material samples were subject to sudden fracture after reaching a yield point corresponding to a 426 N load, and an extension of 2.4 mm, as reported in Table 4.

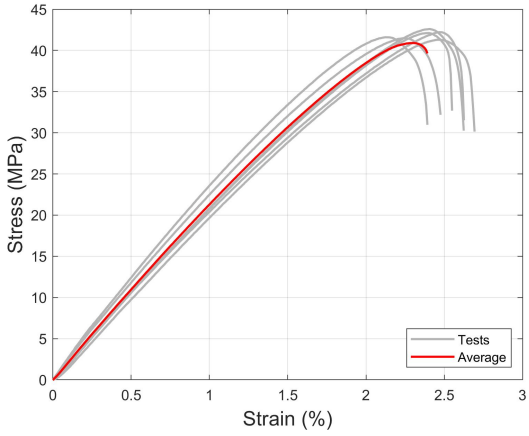


Figure 7. Stress–strain curves for the ABS plastics used in the manufacturing of chiral structures.

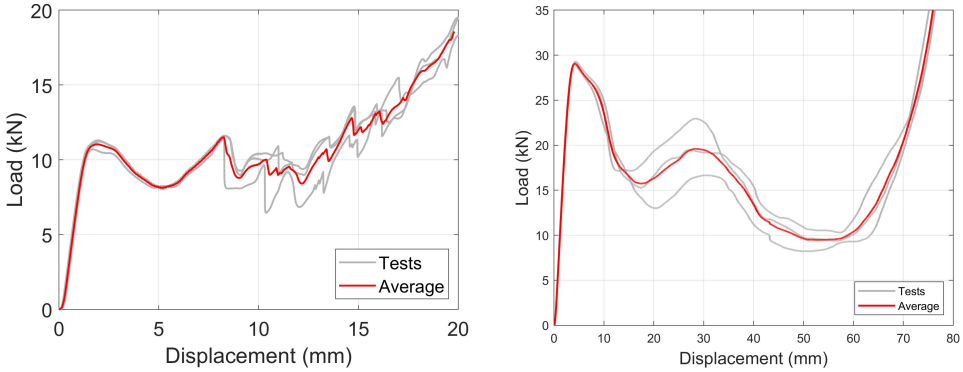
Table 4. Young's modulus, uniaxial tensile strength (MPa) and the maximum strain of the 3D printing specimens.

Young's Modulus (GPa)	Tensile Strength (MPa)	Maximum Strain
2.11 ± 0.25	41.89 ± 0.71	2.56 ± 0.17

3.2. Crushing of Chiral Structures

Chiral lattices are axially and laterally compressed between two rigid plates by using a quasi-static loading. Three specimens were crushed in-plane and out-of-plane directions. The crush properties of the specimens were calculated and presented in Table 5 to show

the scatter and average values. According to the results, a maximum of 15% deviation could be observed in the energy absorption indices, which could be related to the FDM printing ambient conditions such as humidity, sunlight exposure duration and drought in the production room. The SEA values are found as 20.23 J/g and 2.25 J/g for the out-of-plane and in-plane crush of chiral lattices, respectively. The in-plane and out-of-plane load–displacement curves of chiral lattices can be seen in Figure 8a,b.



(**a**) in-plane (**b**) out-of-plane

Figure 8. Load–displacement curves related to the in-plane and out-of-plane crush of chiral lattices.

Table 5. Properties of the chiral structure under in-plane and out-of-plane crushing.

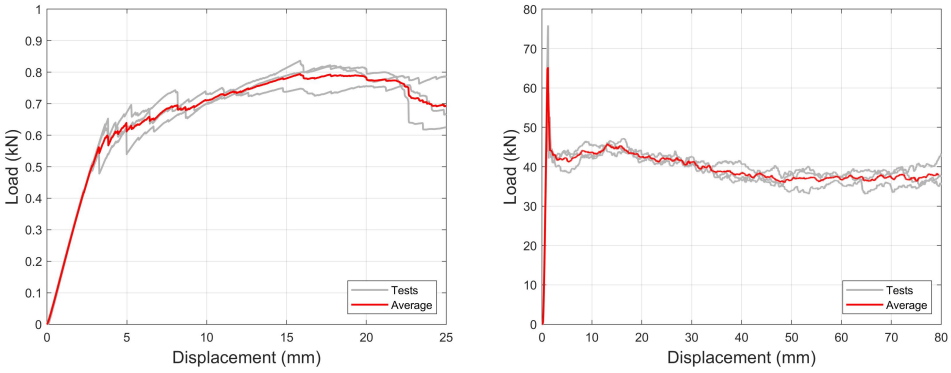
CHIRAL	In-Plane				Out-of-Plane			
	1	2	3	Average	1	2	3	Average
PCF (kN)	11.60	11.39	11.62	11.54 ± 0.15	29.28	28.99	29.01	29.08 ± 0.20
MCF (kN)	9.38	8.44	9.47	9.10 ± 0.66	16.72	16.52	14.20	15.81 ± 1.61
CFE	0.81	0.74	0.82	0.79 ± 0.05	0.57	0.57	0.49	0.54 ± 0.05
AE (kJ)	0.13	0.11	0.13	0.12 ± 0.01	1.17	1.15	0.99	1.10 ± 0.11
SEA (J/g)	2.35	2.06	2.36	2.26 ± 0.20	21.40	21.13	20.23	20.23 ± 2.06

3.3. Crushing of Hollow Tubes

The lateral and uniaxial crush tests for hollow composite tubes are shown in Figure 9a,b, respectively. Three identical composite tubes were used in the tests. The ends of all tubes were cut out to ensure that the tubes are free from burrs or uneven edges. The results are reported in Table 6. The tests were all in good correlation.

Table 6. Properties of the hollow composite tube under lateral and uniaxial crushing.

HOLLOW TUBES	Lateral				Uniaxial			
	1	2	3	Average	1	2	3	Average
PCF (kN)	0.84	0.82	0.76	0.81 ± 0.05	65.16	75.88	75.46	72.17 ± 7.01
MCF (kN)	0.69	0.67	0.64	0.67 ± 0.03	39.86	40.52	38.46	39.61 ± 1.15
CFE	0.82	0.82	0.85	0.83 ± 0.02	0.61	0.53	0.51	0.55 ± 0.06
AE (kJ)	0.017	0.017	0.016	0.017 ± 0.001	3.19	3.22	3.05	3.12 ± 0.10
SEA (J/g)	0.44	0.42	0.41	0.42 ± 0.02	80.91	81.56	77.24	79.90 ± 2.66

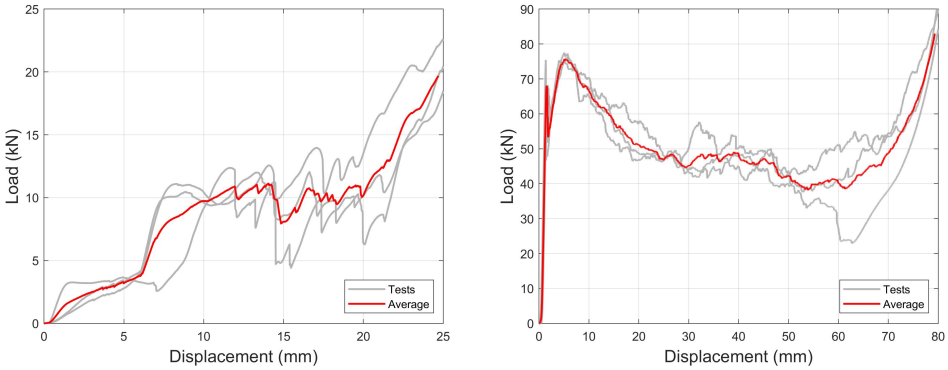


(**a**) lateral (**b**) uniaxial

Figure 9. Load–displacement curves related to the lateral and uniaxial crush of hallow tubes.

3.4. Crushing of Chiral-Filled Tubes

FDM printed chiral structures were placed inside the CFRP composite tubes without using any adhesive to enable the free movement of chiral structures for experiencing the negative Poisson's ratio in the tube. Filled tubes crushed laterally and uniaxially, and the data obtained from the crushed displacement and loadcell output are plotted in Figure 10a,b for the lateral and uniaxial loads, respectively. The scatter of different tests were observed, which can be related to the overlapping effect of both composite tube and chiral structures' scatters. The results are reported in Table 7.



(**a**) lateral (**b**) uniaxial

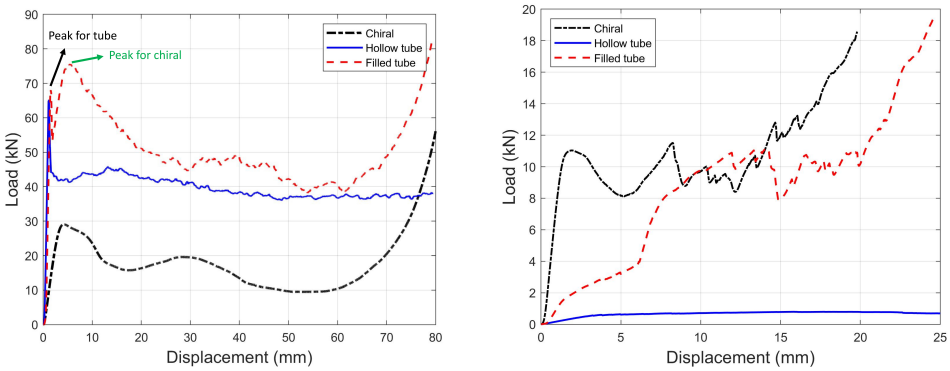
Figure 10. Load–displacement curves related to the lateral and uniaxial crush of chiral-filled tubes.

Table 7. Properties of the chiral-filled tubes under lateral and uniaxial crushing.

FILLED TUBE	Lateral				Uniaxial			
	1	**2**	**3**	**Average**	**1**	**2**	**3**	**Average**
PCF (kN)	12.37	14.55	12.57	13.16 ± 1.39	76.30	77.49	75.32	76.37 ± 1.12
MCF (kN)	6.28	8.34	7.31	7.31 ± 1.03	49.28	51.95	45.31	48.85 ± 3.54
CFE	0.51	0.57	0.58	0.55 ± 0.04	0.65	0.67	0.60	0.64 ± 0.04
AE (kJ)	0.12	0.16	0.15	0.14 ± 0.02	3.45	3.58	3.41	3.48 ± 0.01
SEA (J/g)	1.29	1.74	1.55	1.53 ± 0.24	36.70	38.05	36.24	37.00 ± 1.05

3.5. Comparison of Average Behavior

This section compares the load–displacement behavior and resulting energy absorption characteristics of the chiral structure, the hollow tube and the chiral-filled tube using their average behavior. Uniaxial and lateral crush plots are compared in Figure 11a,b, for the uniaxial and lateral loading respectively. In addition, the average crush properties for chiral structure, hollow tube and filled tube are reported in Tables 8 and 9.



(**a**) uniaxial (**b**) lateral

Figure 11. Load–displacement curves of the lateral and uniaxial crush of chiral structures, hollow tubes and chiral-filled tubes.

Table 8. Average crush properties of the chiral structure, hollow tube and filled tube under uniaxial loading.

UNIAXIAL	PCF (kN)	MCF (kN)	CFE	AE (J)	SEA (J/g)
Chiral	29.09 ± 0.19	15.81 ± 1.61	0.54 ± 0.05	1104.90 ± 110	20.23 ± 2.06
Hollow	72.17 ± 7.01	39.61 ± 1.15	0.55 ± 0.06	3152.97 ± 104.97	79.90 ± 2.66
Filled Tube	76.37 ± 1.12	48.85 ± 3.54	0.64 ± 0.04	3480.23 ± 98.97	37.00 ± 1.05

Table 9. Average crush properties of the chiral structure, hollow tube and filled tube under lateral loading.

LATERAL	PCF (kN)	MCF (kN)	CFE	AE (J)	SEA (J/g)
Chiral	11.54 ± 0.15	9.10 ± 0.66	0.79 ± 0.05	123.20 ± 0.01	2.26 ± 0.20
Hollow	0.81 ± 0.05	0.67 ± 0.03	0.83 ± 0.02	16.70 ± 0.59	0.42 ± 0.02
Filled Tube	13.16 ± 1.39	7.31 ± 1.03	0.55 ± 0.04	143.69 ± 22.35	1.53 ± 0.24

4. Discussion

The base material (ABS) of the chiral structures showed low specific strength and elongation at break values as previously reported in Table 4. The low specific stiffness and strength, and low ductility values directly affected the pre-crushing and progressive crushing stages and caused crush behavior with inadequate performance. The main limitation caused by the material specification of ABS is the prevention of the wrapping mechanism. The premature failure of ligaments while wrapping around the nodes inhibits the auxetic mechanism. The SEA values for out-of-plane crush of chiral lattices were found to be 20.23 J/g and for in-plane, the SEA value was 2.25 J/g. During the in-plane crush process, at first, elastic bending of the ligaments takes place, and it is followed by the bending of the nodes and a fracture of the ligaments and nodes, successively. However, in the out-of-plane loading, local buckling and global buckling can be experienced. In fact, global buckling is an efficient energy-absorbing mechanism, yet it is not preferred due to the instant load drop and the state of instability. This also explains the considerable difference between hollow and filled tube's uniaxial and lateral energy absorption abilities.

In uniaxial loading of hollow and chiral-filled tubes, global buckling and catastrophic failure have not been observed, and the general deformation behavior had characteristics of a progressive failure for the hollow composite tube, which is a desirable failure mechanism [48]. This is provided by the selection of the geometrical parameters to prevent catastrophic failures [19–22]. The similarities between the images shown in Figure 10b and Hull's results [38] for an ideal progressive failure can be easily appreciated. Moreover, the presence of a tearing mode and micro-fragmentation can be seen in Figure 12A–C; these

failure mechanisms were also presented in Bisagni's work [49]. The existence of similar failure modes could also be observed in the chiral-lattice-filled composite tubes, until a specific compression stroke. Beyond that critical value, the chiral lattices expanded laterally and forced the wall of the composite tubes to move radially, which caused a catastrophic failure. That is the reason why no composite tube surrounding chiral lattices is present, and some undeformed large pieces of the composite parts are left at the end of the tests as presented in Figure 12D–F.

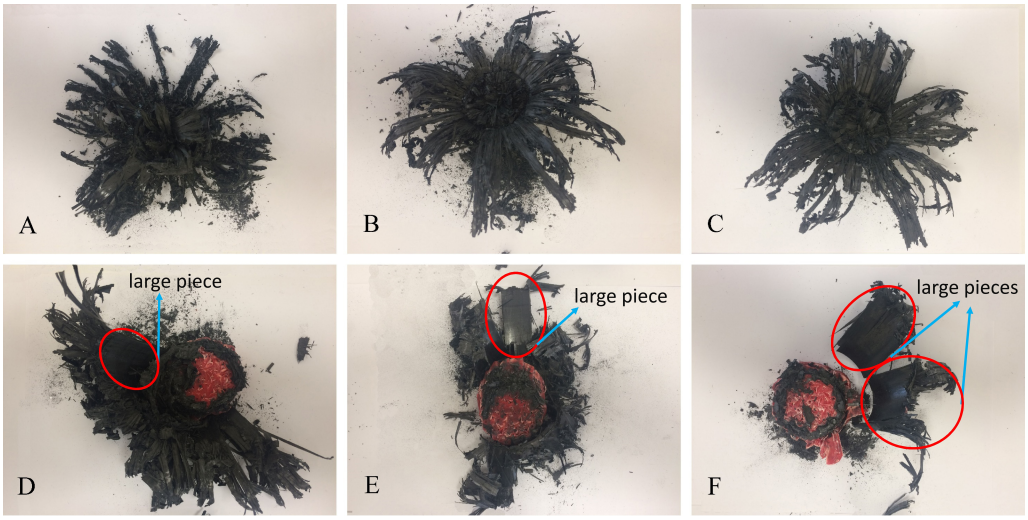


Figure 12. Deformed under uniaxial load. (**A**–**C**) Hollow and chiral; (**D**–**F**) lattice-filled composite tubes.

Observing the load–displacement curves for uniaxially loaded chiral lattices filled composite tubes the densification starts at about 68 mm of compression, and two different peak loads can be observed. The first peak is correlated with the failure of the composite tube; the second one is related to the collapse of the chiral lattices. The curves representing the chiral structure and filled tube showed similar patterns because of the progressive crush of the hollow composite tube.

The use of chiral structure as a filling material for hollow tube increased the PCF and MCF magnitudes in uniaxial loading, as presented in Table 8. An increase in PCF is an undesirable situation for crashworthy structures but the trend in the increase of MCF is more than the PCF. Thus, the CFE value, also known as the load uniformity ratio, reached a value of one, which is an improved performance index. In energy absorption, chiral fillers exhibited higher performance with a 10% increase. However, the addition of extra mass using a chiral structure as a filling material to the configuration provides a small increase in the absorbed energy, although it lowered the SEA value by more than half.

In the case of the lateral (radial) crush of composite tubes, two different energy-absorbing processes occur when the load is applied. One of them is related to the flattening of the tubes cross-sections curvature; the other one is about the presence of hinge lines [47]. The two energy absorption processes could be observed for both the hollow and the chiral-lattice-filled tubes (Figure 13).

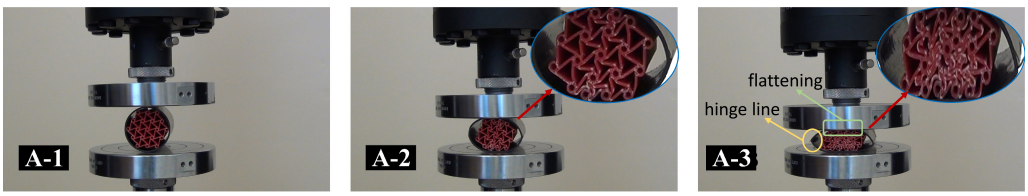


Figure 13. Undeformed (**A-1**), 12.5 mm deflection applied (**A-2**), and 25 mm deflection applied (**A-3**) lattice-filled composite tubes. .

During the lateral compression, both elastic and plastic deformations occur. After the load was removed at the end of the test, it was noticeable how the tube's wall returned close to its original shape. In the last stage of the chiral-filled tube, the diameter of the compressed tube in the uniaxial direction was 25 mm, and it became 44 mm after releasing the load. The final dimensions of the deformed tubes (hollow and chiral lattices-filled) are almost the same (Figure 14). In contrast to the axial compression case, significant in-plane deformation of the chiral lattices auxetic behavior is observed, and the chiral structure does not expand under lateral loads. As seen in Figure 13, the lateral contraction of chiral fillers was experienced, and gaps were formed between composite walls and chiral structures. In Figure 13A-2, the deformation pattern of chiral structure was observed. Nodes started to rotate and ligaments were bent. In Figure 13A-3, it is seen how densification phase started and lateral contraction is increased, in which gaps in the cell was contracted and filled with material. From the observation of Figure 11b, the compression of the hollow composite tubes gives a fairly regular and smooth characteristic load–displacement curve. The shape of the same load–displacement diagram is more irregular in the case of the chiral-filled tubes due to the progressive deformation of the cells in the chiral structures.



Figure 14. Deformed chiral-lattice-filled (**left**) and hollow (**right**) composite tubes under lateral loading.

The lateral crush of the chiral structure and hollow tube do not exhibit distinct peaks or a pre-crushing phase. However, the combination of chiral and hollow tubes enabled the pre-crushing stage and two explicit peaks. Moreover, the onset of the densification phase pulled back to a smaller displacement. According to Table 9, the chiral filler led to a very high increase in the PCF and MCF and decreased CFE values by almost 20%. The absorbed energy by the combination of the chiral structure and hollow tube was higher than the sum of the energies absorbed by constituent elements tested separately. Remarkably, the SEA values were more than three times higher in comparison with that of the hollow tube. This is a clear indication of the negative Poisson's ratio effect of the chiral structures, which creates a large equivalent densification and stiffening effects during transverse compression loading, with only a limited amount of effective mass provided by the filling of the tube. In summary, findings show that the use of chiral lattice fillers provide high performance in which lateral crush of the tubes is targeted, such as helicopter skid landing gears [4]. Additionally, the chiral structure showed better performance in comparison with a hollow tube. However, the chiral structure cannot exhibit negative Poisson's ratio when mounted into the tube due to absence of the free movement. Thus, the use of tube and chiral structure configuration without any adhesive or binder is the optimal way of increasing the performance of the auxetic structure and the composite tube.

5. Conclusions

In this work, tensile and crushing tests were performed on a series of composite CFRP tubes with hollow sections and filled with an auxetic (negative Poisson's ratio) lattice built using a 3D printing technique. Tests on tensile specimens of the representative ABS plastics used to fabricate the auxetic lattices were also performed. The specific energy absorption, the peak load, the average (mean) crushing load, crushing efficiency and stroke efficiency were calculated for different configurations and assessed to understand if auxetic structures could be needed for designing composite crushing tubes.

It was found that adding a chiral lattice filler did not increase the SEA capability of the tubes in the case of uniaxial quasi-static crushing; instead, a significant decrease of

the specific energy absorption was observed. On the other hand, in the case of lateral quasi-static crushing the SEA of the filled tubes increase by 360%, and this is due to the auxetic mechanism triggered during the lateral compression. The peak forces increase slightly under axial compression by using chiral filling structures. The use of these filling structures were found to increase the duration of the crushing force and the total absorbed energy values. The crushing force efficiency of the composite filled crushing tubes under axial compression does increase compared to the case of the hollow tubes. However, the high deformation present when the chiral lattices bottom out could cause some significant lateral outward deformation that pushes against the composite tube walls. The chiral filling material placed in the composite tube significantly increases the peak forces and SEA values during lateral compression.

The use of chiral structures in their prismatic configuration allows benefiting from the negative Poisson's ratio effect and therefore contribute to the artificial stiffening and densification effect that increases the SEA for these composite structures. It should also be emphasized that the findings of this work can be improved if topological parameters of the chiral structure are optimized for maximum energy absorption.

Author Contributions: Conceptualization, K.G.; methodology, K.G.; resources, H.S.T.; writing—original draft preparation, K.G. and A.T.; writing—review and editing, A.T., G.S., H.S.T. and A.M.G.; visualization, K.G.; supervision, H.S.T., G.S. and A.M.G.; funding acquisition, K.G. and H.S.T. All authors have read and agreed to the published version of the manuscript.

Funding: The experimental work of this paper was funded by Istanbul Technical University Industrial Researcher Training Programme (Istanbul Technical University and Republic of Turkey Ministry of Development) grant number ITU-AYP-2016-2. The APC was funded by Imperial College London Open Access Fund.

Institutional Review Board Statement: Not applicable.

Informed Consent Statement: Not applicable.

Data Availability Statement: No data reported.

Conflicts of Interest: The authors declare no conflict of interest.

References

1. Jacob, G.C.; Fellers, J.F.; Simunovic, S.; Starbuck, J.M. Energy absorption in polymer composites for automotive crashworthiness. *J. Compos. Mater.* **2002**, *36*, 813–850. [CrossRef]
2. Zhua, G.; Wanga, Z.; Huoa, X.; Chenga, A.; Lia, G.; Zhoub, C. Experimental and numerical investigation into axial compressive behaviour of thin-walled structures filled with foams and composite skeleton. *Int. J. Mech. Sci.* **2017**, *122*, 104–119. [CrossRef]
3. Jamil, A.; Guan, Z.; Cantwell, W. The static and dynamic response of CFRP tube reinforced polyurethane. *Compos. Struct.* **2017**, *161*, 85–92. [CrossRef]
4. Shrotri, K.; Schrage, D. Composite skid landing gear design feasibility. *J. Am. Helicopter Soc.* **2009**, *54*, 42004–42004. [CrossRef]
5. Hou, T.; Pearce, G.; Prusty, B.; Kelly, D.; Thomson, R. Pressurised composite tubes as variable load energy absorbers. *Compos. Struct.* **2015**, *120*, 346–357. [CrossRef]
6. Yang, K.; Xu, S.; Zhou, S.; Shen, J.; Xie, Y.M. Design of dimpled tubular structures for energy absorption. *Thin-Walled Struct.* **2017**, *112*, 31–40. [CrossRef]
7. Ingrole, A.; Hao, A.; Liang, R. Design and modeling of auxetic and hybrid honeycomb structures for in-plane property enhancement. *Mater. Des.* **2017**, *117*, 72–83. [CrossRef]
8. Shi, L.; Wu, Z.; Cheng, X.; Ru, X.; Yuan, Y. Residual crashworthiness of braided composite tube with transverse multi-impact damages: Experimental and numerical study. *Compos. Struct.* **2021**, *255*, 112903. [CrossRef]
9. Kim, J.; Jeong, M.; Böhm, H.; Richter, J.; Modler, N. Experimental investigation into static and dynamic axial crush of composite tubes of glass-fiber mat/PA6 laminates. *Compos. Part B Eng.* **2020**, *181*, 107590. [CrossRef]
10. Zhu, G.; Yu, Q.; Zhao, X.; Wei, L.; Chen, H. Energy-absorbing mechanisms and crashworthiness design of CFRP multi-cell structures. *Compos. Struct.* **2020**, *233*, 111631. [CrossRef]
11. Caminero, M.; Rodríguez, G.; Muñoz, V. Effect of stacking sequence on Charpy impact and flexural damage behavior of composite laminates. *Compos. Struct.* **2016**, *136*, 345–357. [CrossRef]
12. Asaee, Z.; Taheri, F. Experimental and numerical investigation into the influence of stacking sequence on the low-velocity impact response of new 3D FMLs. *Compos. Struct.* **2016**, *140*, 136–146. [CrossRef]

13. Hongkarnjanakul, N.; Bouvet, C.; Rivallant, S. Validation of low velocity impact modelling on different stacking sequences of CFRP laminates and influence of fibre failure. *Compos. Struct.* **2013**, *106*, 549–559. [CrossRef]
14. Riccio, A.; Di Felice, G.; Saputo, S.; Scaramuzzino, F. Stacking sequence effects on damage onset in composite laminate subjected to low velocity impact. *Procedia Eng.* **2014**, *88*, 222–229. [CrossRef]
15. Saeedifar, M.; Saleh, M.N.; El-Dessouky, H.M.; De Freitas, S.T.; Zarouchas, D. Damage assessment of NCF, 2D and 3D woven composites under compression after multiple-impact using acoustic emission. *Compos. Part A Appl. Sci. Manuf.* **2020**, *132*, 105833. [CrossRef]
16. Saleh, M.N.; Yudhanto, A.; Potluri, P.; Lubineau, G.; Soutis, C. Characterising the loading direction sensitivity of 3D woven composites: Effect of z-binder architecture. *Compos. Part A Appl. Sci. Manuf.* **2016**, *90*, 577–588. [CrossRef]
17. Babbage, J.; Mallick, P. Static axial crush performance of unfilled and foam-filled aluminum–composite hybrid tubes. *Compos. Struct.* **2005**, *70*, 177–184. [CrossRef]
18. Fairful, A. Effects of specimen dimensions on the specific energy absorption of fibre composite tubes. *Proc. ICCM* **1987**, *3*, 36–45.
19. Farley, G.L. Effect of fiber and matrix maximum strain on the energy absorption of composite materials. *J. Compos. Mater.* **1986**, *20*, 322–334. [CrossRef]
20. Farley, G.L. Effect of specimen geometry on the energy absorption capability of composite materials. *J. Compos. Mater.* **1986**, *20*, 390–400. [CrossRef]
21. Hamada, H.; Ramakrishna, S. Scaling effects in the energy absorption of carbon-fiber/PEEK composite tubes. *Compos. Sci. Technol.* **1995**, *55*, 211–221. [CrossRef]
22. Gupta, N.; Velmurugan, R.; Gupta, S. An analysis of axial crushing of composite tubes. *J. Compos. Mater.* **1997**, *31*, 1262–1286. [CrossRef]
23. Liu, Y.; Hu, H. A review on auxetic structures and polymeric materials. *Sci. Res. Essays* **2010**, *5*, 1052–1063.
24. Mir, M.; Ali, M.N.; Sami, J.; Ansari, U. Review of mechanics and applications of auxetic structures. *Adv. Mater. Sci. Eng.* **2014**, *2014*. [CrossRef]
25. Yang, W.; Li, Z-M.; Shi, W.; Xie, B-H.; Yang, M.-B. Review on auxetic materials. *J. Mater. Sci.* **2004**, *39*, 3269–3279. [CrossRef]
26. Deng, S.; Zhang, J.; Ye, L. Halloysite–epoxy nanocomposites with improved particle dispersion through ball mill homogenisation and chemical treatments. *Compos. Sci. Technol.* **2009**, *69*, 2497–2505. [CrossRef]
27. Dirrenberger, J.; Forest, S.; Jeulin, D. Effective elastic properties of auxetic microstructures: anisotropy and structural applications. *Int. J. Mech. Mater. Des.* **2013**, *9*, 21–33. [CrossRef]
28. Grima, J.N.; Chetcuti, E.; Manicaro, E.; Attard, D.; Camilleri, M.; Gatt, R.; Evans, K.E. On the auxetic properties of generic rotating rigid triangles. *Proc. R. Soc. A Math. Phys. Eng. Sci.* **2012**, *468*, 810–830. [CrossRef]
29. Chen, Y.; Scarpa, F.; Liu, Y.; Leng, J. Elasticity of anti-tetrachiral anisotropic lattices. *Int. J. Solids Struct.* **2013**, *50*, 996–1004. [CrossRef]
30. Liu, W.; Wang, N.; Huang, J.; Zhong, H. The effect of irregularity, residual convex units and stresses on the effective mechanical properties of 2D auxetic cellular structure. *Mater. Sci. Eng. A* **2014**, *609*, 26–33. [CrossRef]
31. Ma, Y.; Scarpa, F.; Zhang, D.; Zhu, B.; Chen, L.; Hong, J. A nonlinear auxetic structural vibration damper with metal rubber particles. *Smart Mater. Struct.* **2013**, *22*, 084012. [CrossRef]
32. Günaydin, K.; Eren, Z.; Scarpa, F. Experimental investigation of auxetic structures subjected to quasi static axial load. In Proceedings of the 2017 8th International Conference on Recent Advances in Space Technologies (RAST), Istanbul, Turkey, 19–22 June 2017; pp. 7–10.
33. Günaydın, K.; Eren, Z.; Kazancı, Z.; Scarpa, F.; Grande, A.M.; Türkmen, H.S. In-plane compression behavior of anti-tetrachiral and re-entrant lattices. *Smart Mater. Struct.* **2019**, *28*, 115028. [CrossRef]
34. Zhang, X.C.; Ding, H.M.; An, L.Q.; Wang, X.l. Numerical investigation on dynamic crushing behavior of auxetic honeycombs with various cell-wall angles. *Adv. Mech. Eng.* **2015**, *7*, 679678. [CrossRef]
35. Mohsenizadeh, S.; Alipour, R.; Nejad, A.F.; Rad, M.S.; Ahmad, Z. Experimental investigation on energy absorption of auxetic foam-filled thin-walled square tubes under quasi-static loading. *Procedia Manuf.* **2015**, *2*, 331–336. [CrossRef]
36. Fíla, T.; Zlámal, P.; Jiroušek, O.; Falta, J.; Koudelka, P.; Kytýř, D.; Doktor, T.; Valach, J. Impact Testing of Polymer-filled Auxetics Using Split Hopkinson Pressure Bar. *Adv. Eng. Mater.* **2017**, *19*, 1700076. [CrossRef]
37. Simpson, J.; Kazancı, Z. Crushing investigation of crash boxes filled with honeycomb and re-entrant (auxetic) lattices. *Thin-Walled Struct.* **2020**, *150*, 106676. [CrossRef]
38. Hull, D. A unified approach to progressive crushing of fibre-reinforced composite tubes. *Compos. Sci. Technol.* **1991**, *40*, 377–421. [CrossRef]
39. Elgalai, A.M.; Mahdi, E.; Hamouda, A.; Sahari, B. Crushing response of composite corrugated tubes to quasi-static axial loading. *Compos. Struct.* **2004**, *66*, 665–671. [CrossRef]
40. Li, Q.; Magkiriadis, I.; Harrigan, J.J. Compressive strain at the onset of densification of cellular solids. *J. Cell. Plast.* **2006**, *42*, 371–392. [CrossRef]
41. Caulfield, B.; McHugh, P.E.; Lohfeld, S. Dependence of mechanical properties of polyamide components on build parameters in the SLS process. *J. Mater. Process. Technol.* **2007**, *182*, 477–488. [CrossRef]
42. Chua, C.; Feng, C.; Lee, C.; Ang, G. Rapid investment casting: direct and indirect approaches via model maker II. *Int. J. Adv. Manuf. Technol.* **2005**, *25*, 26–32. [CrossRef]

43. Upcraft, S.; Fletcher, R. The rapid prototyping technologies. *Assem. Autom.* **2003**, *23* 318–330.. [CrossRef]
44. Alderson, A.; Alderson, K.L.; Attard, D.; Evans, K.E.; Gatt, R.; Grima, J.N.; Miller, W.; Ravirala, N.; Smith, C.; Zied, K. Elastic constants of 3-, 4-and 6-connected chiral and anti-chiral honeycombs subject to uniaxial in-plane loading. *Compos. Sci. Technol.* **2010**, *70*, 1042–1048. [CrossRef]
45. Prall, D.; Lakes, R. Properties of a chiral honeycomb with a Poisson's ratio of −1. *Int. J. Mech. Sci.* **1997**, *39*, 305–314. [CrossRef]
46. ISO. *527–1:2012 Plastics–Determination of Tensile Properties*; ISO: Geneva, Switzerland, 2012.
47. Elahi, S.A.; Rouzegar, J.; Niknejad, A.; Assaee, H. Theoretical study of absorbed energy by empty and foam-filled composite tubes under lateral compression. *Thin-Walled Struct.* **2017**, *114*, 1–10. [CrossRef]
48. Shin, K.C.; Lee, J.J.; Kim, K.H.; Song, M.C.; Huh, J.S. Axial crush and bending collapse of an aluminum/GFRP hybrid square tube and its energy absorption capability. *Compos. Struct.* **2002**, *57*, 279–287. [CrossRef]
49. Bisagni, C. Experimental investigation of the collapse modes and energy absorption characteristics of composite tubes. *Int. J. Crashworthiness* **2009**, *14*, 365–378. [CrossRef]